Bacterial-Cellulose-Derived Carbon Nanofiber@MnO 2 and Nitrogen-Doped Carbon Nanofiber Electrode Materials: An Asymmetric Supercapacitor with High Energy and Power Density

5 AUTHORS, INCLUDING:

Shu-Hong Yu

University of Science and Technology of Ch…

367 PUBLICATIONS **15,029** CITATIONS

Bacterial Cellulose Derived Carbon Nanofiber@MnO₂ and Nitrogen-Doped Carbon Nanofiber Electrode Materials: Asymmetric Supercapacitor with High Energy and Power Density**

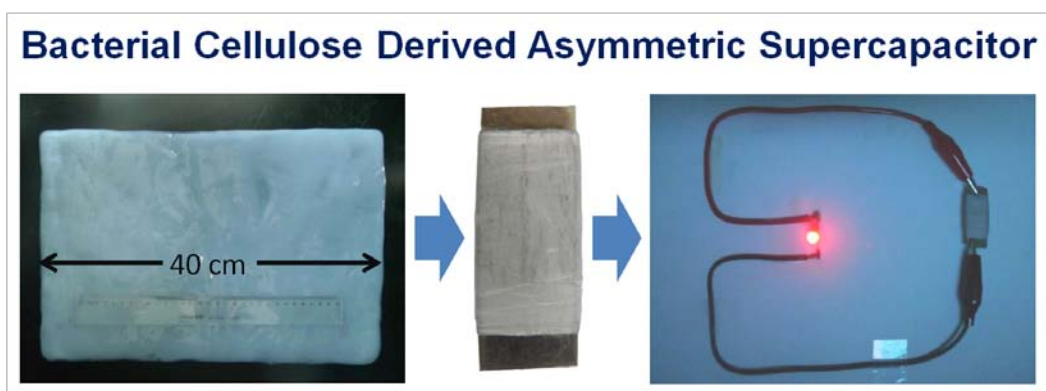By *Li-Feng Chen, Zhi-Hong Huang, Hai-Wei Liang, Qing-Fang Guan, Shu-Hong Yu**

_____

[*] Prof. S.H. Yu, Dr. L.F. Chen, Z.H. Huang, H.W. Liang, Q.F. Guan
Division of Nanomaterials and Chemistry, Hefei National Laboratory for Physical Sciences at Microscale, Department of Chemistry, University of Science and Technology of China, Hefei, Anhui 230026, China
E-mail: shyu@ustc.edu.cn. Fax: +86 551 3603040

Supporting Information is available from the Wiley Online Library or from the author.

Table Content Used Only:

High performance asymmetric supercapacitor: a new kind of high-performance asymmetric supercapacitor has been designed with pyrolyzed bacterial cellulose (p-BC) coated MnO_2 as positive electrode material and nitrogen-doping p-BC as negative electrode material *via* an easy, efficient, large-scale, and green fabrication approach (see Figure). The optimal asymmetric device possesses an excellent supercapacitive behavior with quite high energy and power density.

Nowadays, supercapacitor has drawn extensive attentions because they can instantaneously transport higher power within a very short period than rechargeable batteries and possess higher energy density than conventional dielectric capacitors,[1] which makes them promising for applications such as backup/auxiliary power sources of electric vehicles and stand-by power systems.[2-5] However, commercial supercapacitors suffer from a low energy density;[2, 6] and certain fields such as load-leveling and large industrial equipment need supercapacitors with higher energy and power density to optimize their performance.[7,8] Therefore, it is essential to improve the energy density of the supercapacitor significantly for meeting the pressing requirements.

For a long period, a great deal of work has been done to enhance energy density by extending the operating voltage using organic electrolyte or electrode materials with large capacitances in the symmetric supercapacitor.[9-11] Nevertheless, the organic media inevitably increases the equivalent series resistance compared with aqueous media, leading to relatively low power density.[12] Moreover, some organic media are expensive, flammable, or highly toxic.[13] Then, various categories of redox-reaction materials, including metal oxides, conductive polymers and hybrid materials,[14] have been employed as electrodes to improve the energy density dramatically. Among them, MnO_2 exhibiting low cost, environmental compatibility, and high theoretical pseudo-capacitance, has attracted intense attentions.[15,16] However, the low conductivity of MnO_2 ($10^{-5}-10^{-6}$ S·cm^{-1}) results in a poor charge/discharge rate for high-power applications.[17] To improve the electrical conductivity, researchers developed approaches of compositing nanosized MnO_2 with carbon materials, including carbon nanofoams,[18,19] carbon nanotubes,[7] graphene.[20,21] Unfortunately, the carbon/MnO_2-based capacitor only shows ideal capacitive behavior in aqueous electrolytes, where the potential window is relatively small, and consequently deliver limited energy or power densities.[22] The best way to solve

this problem is to utilize an effective strategy of the asymmetric system by coupling different positive and negative electrode materials with well-separated potential windows to obtain a high operation voltage, thus producing a large energy and power densities.[4,22,23] The key points in achieving ultrahigh energy and power densities are to design appropriate materials (especially nanostructured containing-carbon materials) as Faradic electrode and to select suitable capacitive electrode materials (usually carbon materials).[2,6,23] Although the present containing-carbon asymmetric supercapacitors exhibit good properties,[5,6, 12, 24] preparation processes of some relevant materials (hazardous, awkward, time-consuming, or high-cost) limit their widespread application. Thus, it urgently demands for developing relatively simple, cost-effective and green approaches.

Bacterial cellulose (BC), a low-cost, environmentally friendly, and abundant resource, can be produced on industrial scales *via* microbial fermentation process,[25,26] furthermore, pyrolyzed BC pellicles (*p*-BC) composed of interconnected nanowires has been used to prepare graphitized films and carbon nanofibers.[26,27] Inspired by these facts, here we construct an asymmetric supercapacitor containing a three-dimensional (3D) *p*-BC nanofiber network coated MnO_2 (*p*-BC@MnO_2) as positive electrode prepared by a redox at room temperature and nitrogen-doped *p*-BC (*p*-BC/N) nanomaterial as negative electrode derived from *p*-BC and urea *via* a facile hydrothermal reaction under mild condition. The optimized device can be reversibly charged/discharged at a voltage of 2.0 V in 1.0 M Na_2SO_4 solution, reaching a considerably high energy density of 32.91 Wh·kg^{-1} and maximum power density of 284.63 kW·kg^{-1}. Meanwhile, the supercapacitor exhibits good cycling durability with 95.4% specific capacitance retained after 2000 cycles. More importantly, the electrode materials have unique characteristics, such as low cost and easy fabrication.

Since the pseudo-capacitance of MnO_2 dominantly determines from the surface Faradic

reactions,[15] it has been greatly desirable to prepare MnO_2 nanostructures with an ultrathin morphology. Hence, we coated the carbon nanofibers with the MnO_2 nanofilm, which provided a high electrochemically active surface area for redox Faradic reaction.[12]
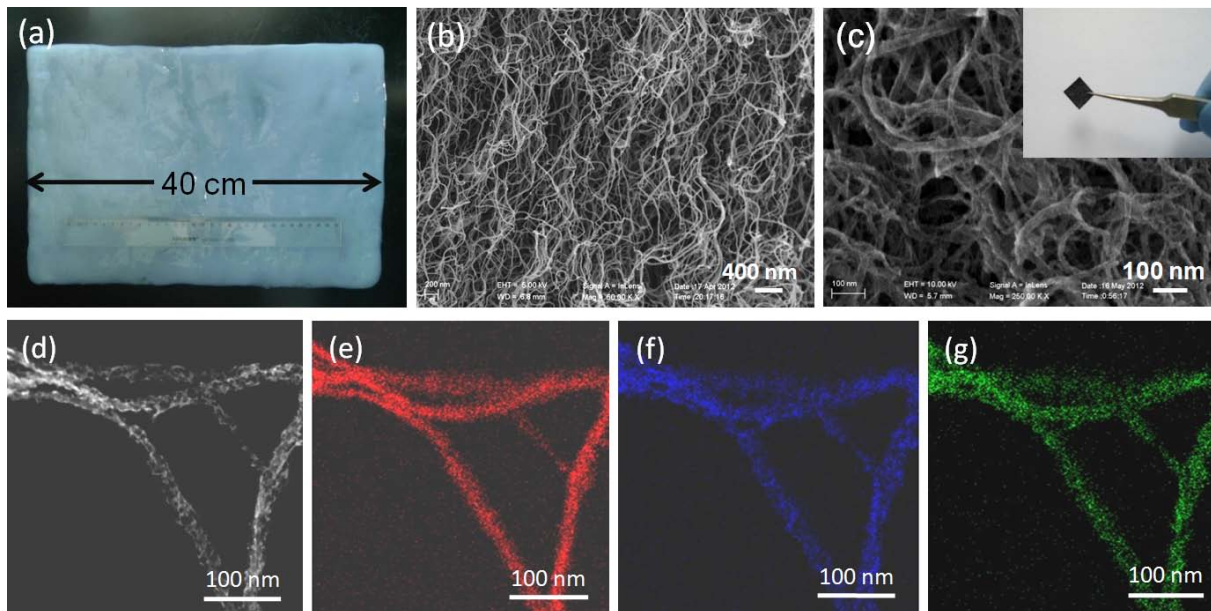
Figure 1. (a) Photograph of the pristine material BC pellicle. (b) SEM image of *p*-BC. (c) SEM image of *p*-BC@MnO$_2$-2h (inset: photograph of *p*-BC@MnO$_2$-2h). (d-g) STEM image of *p*-BC@MnO$_2$-2h with corresponding elemental mapping images of (e) C, (f) Mn, and (g) O.

The BC pellicles (**Figure 1**a) were employed as raw materials to fabricate nanofibrous 3D carbon network *p*-BC *via* annealing at 1000 °C for 2.0 h in N_2. Then, the *p*-BC pellicles were immersed into 0.1 M $KMnO_4$/0.1 M K_2SO_4 aqueous solution to obtain the product *p*-BC@MnO$_2$ nanocomposites. Different amounts of MnO_2 can easily coat on the *p*-BC only by controlling reaction time, leading to samples denoted here as *p*-BC@MnO$_2$-xh (x = 0.5, 1.5, 2.0, 2.5). Increasing reaction time, significantly increase of MnO_2 deposited on the *p*-BC is observed by the analysis of inductively coupled plasma-atomic emission spectrometry (ICP-AES): the mass percentage of MnO_2 with dipping time of 0.5, 1.5, 2.0, and 2.5 h is 13.24±0.14, 26.83±0.27, 34.32±0.34, and 38.56±0.39 wt %, respectively. It suggests that MnO_4^- ions can be reduced spontaneously to MnO_2 on the surface of *p*-BC by oxidizing exterior carbon based on the redox reaction: $4MnO_4^- + 3C + H_2O \rightarrow 4MnO_2 +$

5

$CO_3^{2-} + 2HCO_3^-$. This is a highly efficient green synthesis without adding any poisonous agents; moreover, it proceeds in a neutral mild condition. Consequently, the *p*-BC@MnO$_2$-2h still maintains the initial structure of *p*-BC pellicle (inset in Figure 1c).
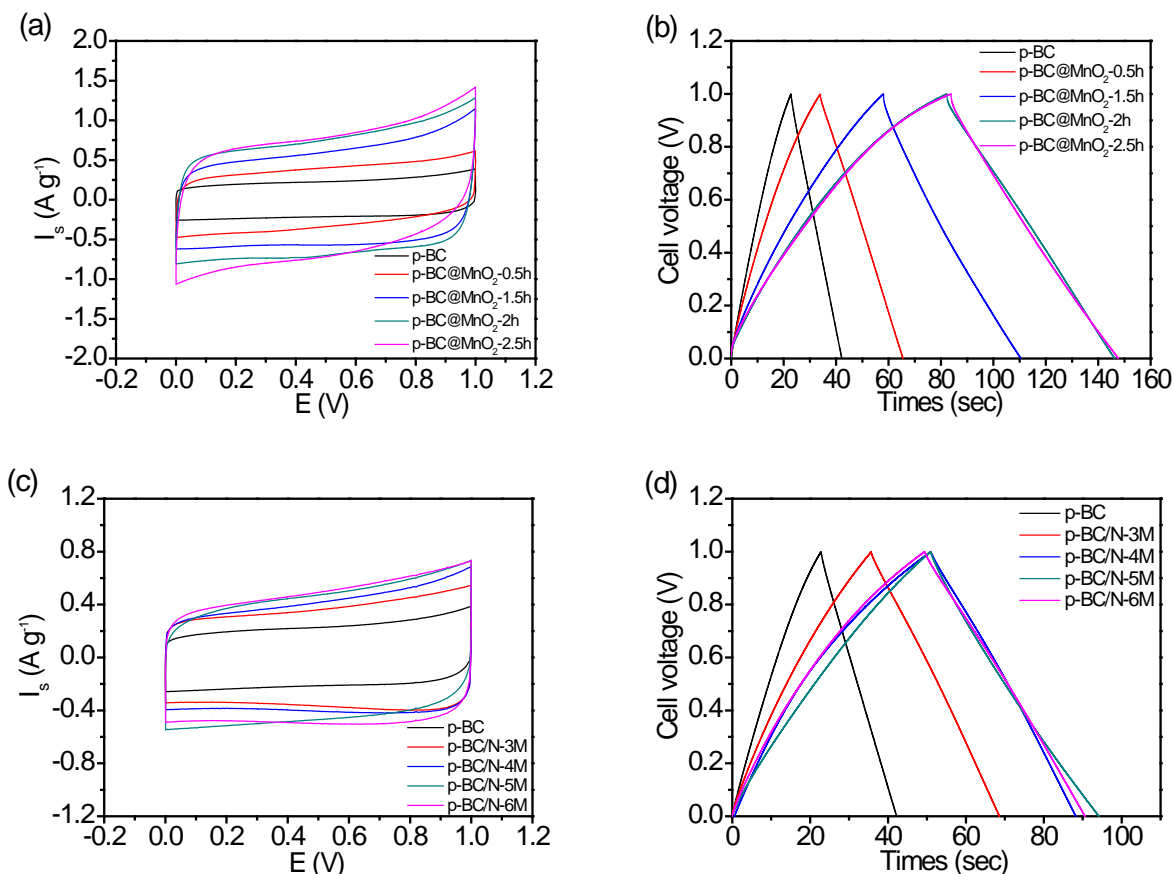
Figure 2. Electrochemical properties of the materials measured using a two-electrode system in 1.0 M Na$_2$SO$_4$ aqueous electrolyte. a) Cyclic voltammetry (CV) curves of *p*-BC@MnO$_2$ and *p*-BC at the scan rate of 10 mV s^{-1}. b) Charge-discharge curves of *p*-BC@MnO$_2$ and *p*-BC at the current density of 1.0 A g^{-1}. c) CV curves of *p*-BC/N and *p*-BC at the scan rate of 10 mV s^{-1}. d) Charge-discharge curves of *p*-BC/N and *p*-BC at the current densities of 1.0 A g^{-1}.

Scanning electron microscopy (SEM) image of *p*-BC (Figure 1b) displays that the as-pyrolyzed BC pellicle has a network structure with 10–20 nm nanowires and many interconnected pores, where void volume allows MnO$_4^-$ ions to diffuse into the pellicle and be reduced to MnO$_2$ on the surface of the nanofibers. After deposition of MnO$_2$ the nanocomposite still maintains a 3D structure consisting of coadjacent nanowires (Figure 1c). Furthermore, there are no obvious agglomerates of MnO$_2$ on the

exterior of *p*-BC pellicle (see Supporting Information Figure S1). More importantly, the scanning transmission electron microscopy (STEM) and X-ray elemental mappings (Figure 1d–g) prove that the MnO_2-covering *p*-BC was successfully fabricated by the spontaneous reduction deposition process, meanwhile, suggested homogeneous, nanoscale of manganese oxide is distributed throughout the *p*-BC pellicle. Moreover, during the preparation of the STEM specimen, MnO_2 nanoparticles are still incorporated on the surface of *p*-BC after a long time sonication, implying the strong interaction between MnO_2 nanofilms and *p*-BC nanowire. From the above discussion, it is found that the MnO_2 nanofilm intimately connected with the *p*-BC nanowires and uniformly distributed throughout the *p*-BC pellicles.

Then, X-ray photoelectron spectroscopy (XPS) was used to identify the presence and oxidation state of the as-synthesized MnO_2 covering *p*-BC. The survey XPS spectrum of *p*-BC@MnO_2-2h confirms the co-existence of Mn, C, and O elements (see Supporting Information Figure S2a). And the Mn 2p spectrum suggests the formation of manganese oxides. Meanwhile, the *p*-BC@MnO_2-2h exhibits a peak separation value of 4.8 eV for the Mn 3s (Supporting Information Figure S2c), indicating the Mn^{4+} is dominant in the product.[7, 28] Next, the crystal phase of MnO_2 in the products was analyzed by X-ray diffraction (XRD) (Supporting Information). The XRD pattern suggested *p*-BC@MnO_2-xh consists of MnO_2 (JCPDS 42-1317) and graphitized carbon.[12] In addition, for the *p*-BC@MnO_2, with the increase of dipping time of *p*-BC in $KMnO_4$/K_2SO_4 solution, the intensity of the peak at around 37° gradually enhances due to more MnO_2 loaded on the *p*-BC nanowires. These results were also revealed by Raman spectrum (see Supporting Information Figure S3b). The G-band in the first-order Raman spectra is sharper and stronger than the D-band, indicating a high graphitization of *p*-BC.[8, 12] The relative intensity of MnO_2 peaks to C peaks suggests a gradual increase of MnO_2 loaded on *p*-BC with

the prolongation of dipping time. These results also revealed that the presence of p-BC as carbon source in the redox reaction results in the formation of MnO_2 coating on p-BC nanowires. The N_2 adsorption−desorption isotherms and pore size distribution curves reveal the p-BC exhibits the coexistence of micropores and mesopores,[8] while the product p-BC@MnO_2-2h possesses a large sum of mesopores (see Supporting Information Figure S4). Such mesoporous structure allows fast diffusion of electrolyte ions owing to the reduced solid-state transport length. The porous properties of these materials were summarized in Table S1 (Supporting Information).

In the following step, the capacitive performances of p-BC@MnO_2-xh composites were evaluated by a two-electrode system with a symmetric supercapacitor p-BC@MnO_2-xh//p-BC@MnO_2-xh in 1.0 M Na_2SO_4 aqueous electrolyte. To fabricate the symmetric device, the p-BC@MnO_2-xh was cut into slices (1.0 × 1.0 cm) as the electrode material without using any binding agents and/or conducting additives. The CV curves of p-BC/p-BC and p-BC@MnO_2-0.5h//p-BC@MnO_2-0.5h are similar to quasi-rectangle and exhibit near mirror-image symmetry (**Figure 2**a), demonstrating the ideal capacitive behavior. And the CV curves exhibits larger rectangle with the increase of dipping time of p-BC in $KMnO_4$/K_2SO_4 aqueous solution. The galvanostatic charge/discharge curves of the p-BC@MnO_2-xh//p-BC@MnO_2-xh at a current density of 1.0 A g^{-1} (Figure 2b) are nearly linear and symmetrical without obvious *IR* drop, suggesting a rapid and reversible Faradic reaction between Na^+ and the ultrathin MnO_2.[12] The homogeneous distribution of the MnO_2 is crucially important for increasing the electrochemical capacitance of the nanocomposites without increasing charge transfer or contact resistance[19] Because formed MnO_2 nanofilm is on the surface of p-BC, the capacitance of p-BC@MnO_2-xh//p-BC@MnO_2-xh is much larger than that of p-BC//p-BC (77.76 F·g^{-1}). Prolonging the dipping time from 0.5 h to 1.5 h, then to 2.0 h leads to a significant increase of the specific

capacitance (C_s) for the electrode material (at 1.0 A·g^{-1}) from 139.78 F·g^{-1} to 213.32 F·g^{-1}, then to 254.64 F·g^{-1}, owing to the increase of the incorporating pseudocapacitive material into the 3D porous network. And the C_s slightly enhances to 256.74 F g^{-1} at the dipping time of 2.5 h because most of the pseudo-capacitance charge is mainly transferred at the surface or in the bulk near surface of the electrode material. [15] Hence, we plan to employ p-BC@MnO$_2$-2h as the positive material of our asymmetry supercapacitor. Additionally, the C_s of p-BC@MnO$_2$-2h is much higher than that of MnO$_2$ nanoflowers grown on carbon nanotube (CNT) arrays (199.0 F·g^{-1})[29] and comparable to that of MnO$_2$ incorporated within activated graphene.[24]

The rate capability is a key for the supercapacitor,[8] hence we plotted the C_s of p-BC and p-BC@MnO$_2$-xh at different current densities. Clearly, the rate capability shows a slight decrease with the increase of dipping time (see Supporting Information Figure S5a), which is attributed to a little reduced access of the electrolyte to the composite with a higher content of MnO$_2$.[12] Nevertheless, the p-BC@MnO$_2$-2h nanocomposite still presents a good rate capacity as the uniform MnO$_2$ nanofilm plays an important role in fast electron propagation during the charge/discharge at high current densities.[30] For example, its C_s maintains as high as 197.42 F·g^{-1} at a rate of 10 A·g^{-1}, 77.53 % retention of 1.0 A·g^{-1}, which is larger than that of the MnO$_2$ nanofibers grown on graphitic hollow carbon spheres (GHCS-MnO$_2$) (144.0 $vs.$ 101.0 F·g^{-1} as the current density increases from 1.0 to 10 A·g^{-1}).[12] Moreover, its rate capability can be comparable to that of the multiwall carbon nanotube/MnO$_2$ (MWNT/MnO$_2$)[7] and graphene/MnO$_2$.[5]

The good electrochemical performances of p-BC@MnO$_2$-2h can be ascribed to its unique nanostructure; the low-cost p-BC substrate with high graphitization serves as a highly conductive matrix for fast ion and electron transport, while the ultrathin MnO$_2$ film strongly anchoring on the

surface of *p*-BC nanowires can effectively reduce the diffusion length of electrolyte ions during the charge/discharge process and provide a large electrochemically active surface area for the fast reversible Faradic redox reactions.[12, 23]

Our recent research revealed the nitrogen-doped carbon nanofiber as the electrode material of supercapacitor can enlarge the capacitance.[8] Therefore, nitrogen-doped *p*-BC (*p*-BC/N) may be a highly promising candidate for the cathode material of an asymmetric supercapacitor. Subsequently, we used *p*-BC as a precursor to synthesize the *p*-BC/N only through a simple hydrothermal reaction.
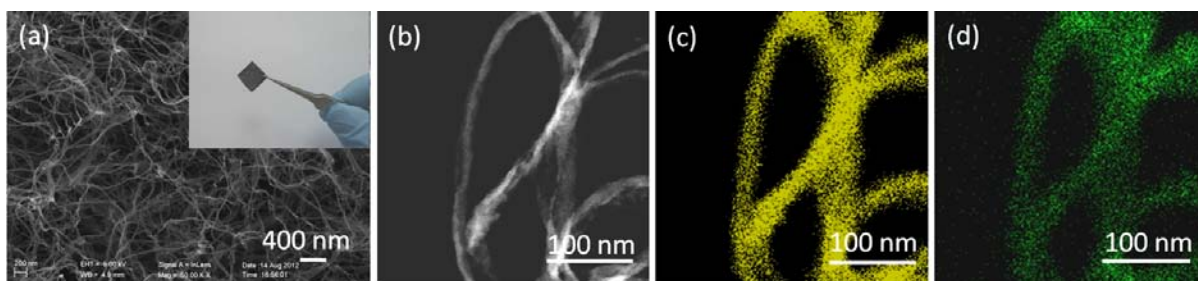
Figure 3. (a) SEM image of *p*-BC/N-5M (inset: photograph of *p*-BC/N-5M). (b) Typical STEM image of *p*-BC/N-5M. (c, d) Corresponding elemental mapping images of (c) C and (d) N.

The typical *p*-BC/N denoted as *p*-BC/N-5M was synthesized by a hydrothermal reduction with 40 mg *p*-BC pellicle and 40.0 mL of 5.0 M urea aqueous solution at 180 °C for 12 h; in the preparation process, the urea aqueous solution can easily permeate through the *p*-BC, thus the product can be prepared *via* the hydrothermal reaction on a large scale. The as-prepared *p*-BC/N-5M still maintains a free-standing 3D pellicle (**Figure 3**a) with overlapped nanowires and cross-linking pores (Figure 3a). The STEM revealed the *p*-BC/N-5M possesses network structure consisting of 10−20 nm nanowires (Figure 3b). Moreover, elemental mapping of *p*-BC/N-5M demonstrated the uniform doping of nitrogen (Figure 3c,d).
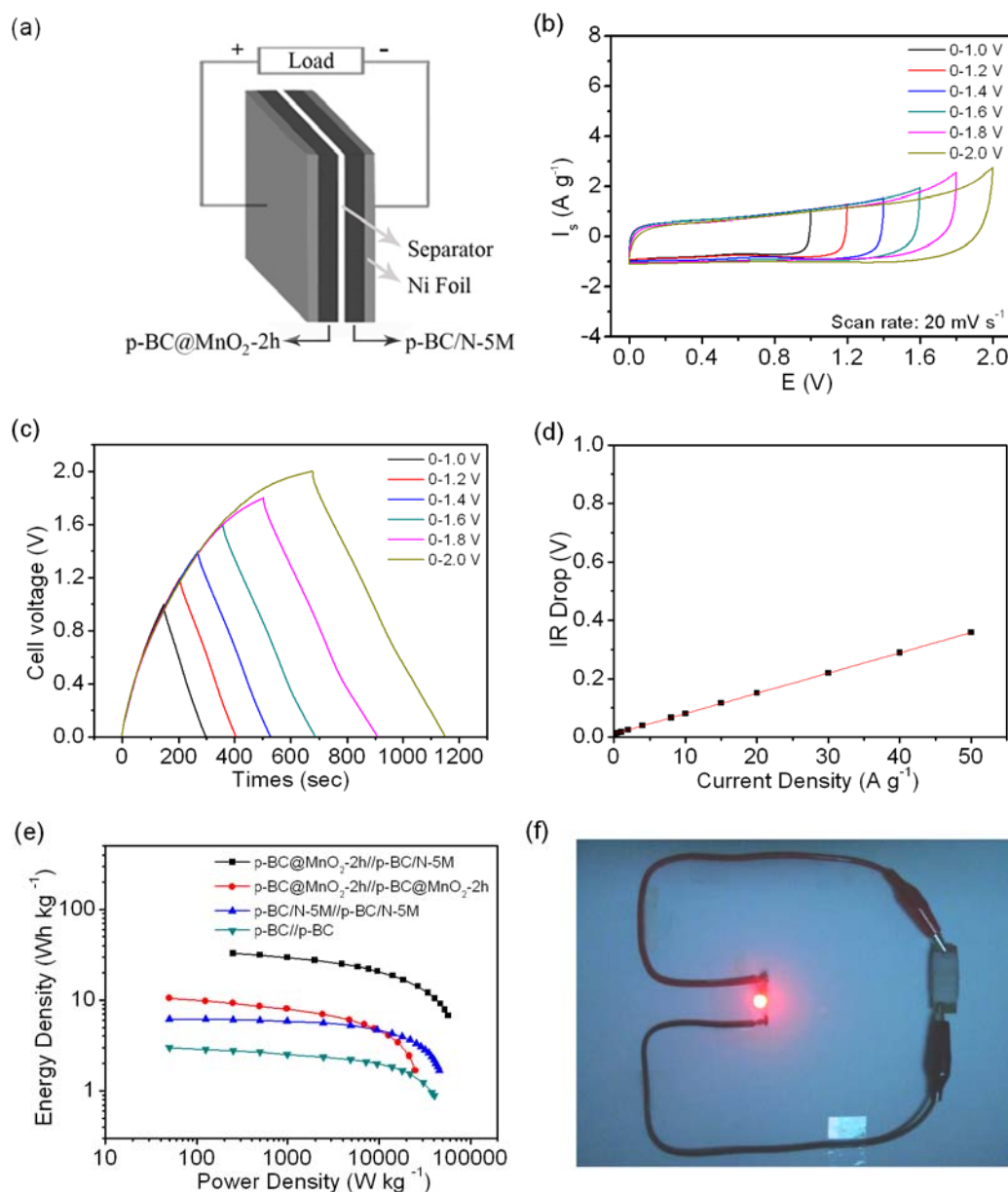
Figure 4. Capacitive performances of the asymmetric supercapacitor (p-BC@MnO$_2$-2h//p-BC/N-5M) with p-BC@MnO$_2$-2h as positive electrode and p-BC/N-5M as negative electrode in 1.0 M Na$_2$SO$_4$ aqueous electrolyte. (a) Scheme of our asymmetric supercapacitor device. (b) CV curves of different operation voltages at the scan rate of 20 mV s^{-1}. (c) Galvanostatic charge–discharge curves of different operation voltages at a current density of 0.25 A g^{-1}. (d) Potential drop (V_{drop}) at different discharge current densities. e) Ragone plots of the supercapacitors. (f) Digital image of a red light-emitting diode (LED) lighted by the p-BC@MnO$_2$-2h//p-BC/N-5M device.

To evaluate the nitrogen functionalities of p-BC/N-5M, XPS was carried out. The doping of nitrogen changes the number and type of surface species (see Supporting Information Figure S6a); N 1s peak is no obvious for p-BC, however, the high-resolution one in the p-BC/N-5M can be divided

into three forms of functional groups (see Supporting Information Figure S6b), namely, pyridinic (N-6, 398.1±0.2 eV), pyrrolic/pyridine (N-5, 400.0±0.2 eV), and quaternary nitrogen (N-Q, 401.0±0.2 eV),[8] indicating there are a great many nitrogen atoms. Accordingly, the low-temperature hydrothermal reaction between the *p*-BC and urea may be an effective method to introduce surface functionalities into carbon materials. The plentiful N-containing species (especially, N-6 and N-Q, 5.15 atom %) would serve as electrochemically active sites for improving the capacitive properties of the materials.[8, 31]

After doping nitrogen, there is a decrease in the surface area and volume of micropores owing to the destruction of pore walls and micropore blocking by functional groups.[32] *p*-BC/N-5M still exhibits a high S_{BET} (252.23 m^2·g^{-1}) with a large number of mesopores (see Supporting Information Figure S7). The pore parameters of this material were also summarized in Table S1 (Supporting Information). The preserved porous network and high mesopore ratio are profitable to the transport and diffusion of electrolyte ions during the fast charge/discharge process, facilitating high-quality performance of the supercapacitor.[5]

In order to demonstrate *p*-BC/N-5M is an optimal N-doping *p*-BC as the electrode material of supercapacitors, the controlled samples, *p*-BC/N-yM (y denoted as the molarity of urea in aqueous solution, y = 3, 4, 6), were synthesized only by adjusting the concentration of urea solution in the reaction. The electrochemical tests of the *p*-BC/N were also performed *via* a two-electrode system in 1.0 M Na$_2$SO$_4$ aqueous electrolyte. CV curves of *p*-BC/N//*p*-BC/N are relatively rectangular-like shapes and display near mirror-like images (Figure 2c), which suggested the supercapacitor possesses ideal capacitive behavior and a good reversibility.[33] The appearance of a few humps in CV curves was owing to the redox reactions of electrochemically active functionality groups on the surface of

electrode,[8] thus it follows that the capacitive response of the *p*-BC/N//*p*-BC/N is contribution of electric double-layer capacitance (EDLC) and redox reactions. Moreover, C_s of *p*-BC/N-5M calculated from galvanostatic charge/discharge curves (Figure 2d) is 173.32 F·g^{-1}, much larger than that of *p*-BC (only 77.70 F·g^{-1}). Previous research[32] has shown that the large C_s can be ascribed to proper surface functionalities, high nitrogen level, and appropriate nitrogen species. Figure S5b depicts the relationship between the C_s of *p*-BC/N and discharge current density (Supporting Information). Obviously, the C_s value of *p*-BC/N-5M is much larger than that of *p*-BC/N-yM at same current density; furthermore, *p*-BC/N-5M possesses a good rate capability than other *p*-BC/N-yM (the C_s of *p*-BC/N-5M is still as high as 136.68 F g^{-1} even at a high current density of 50 A·g^{-1}). As a result, we chose *p*-BC/N-5M as the negative material of the following asymmetric supercapacitor. The good electrochemical performance of *p*-BC/N-5M can be attributed to high-content nitrogen doping and proper nitrogen species, which can improve the capacitance, electrical conductivity, and the wettability in the electrolyte.[8] In addition, the interconnected pore structure and high specific surface area of *p*-BC/N-5M increase the accessibility for electrolyte ion diffusion and transport.[31,32]

Then, we fabricated an asymmetric supercapacitor using *p*-BC@MnO$_2$-2h as positive electrode material and *p*-BC/N-5M as negative material with 1.0 M Na$_2$SO$_4$ aqueous electrolyte. Referring to previous reports, the MnO$_2$-based carbon material is electrochemically stable within a potential window of 0–1.0 V (*vs*. Ag/AgCl) [5] and the nitrogen-doping carbon material displays a good electrochemical stability in electrolyte of 1.0 M Na$_2$SO$_4$ aqueous solution within −1.0–0 V (*vs*. Ag/AgCl).[32] [5] Therefore, the working voltage of the designed asymmetric device (**Figure 4**a, and also see Supporting Information Figure S8) can extend up to 2.0 V.[13, 34] The mass ratio of positive electrode (0.6 mg) to negative electrode (0.9 mg) was fixed close to 0.68 on the basis of charge balance

theory.[23] Figure 4b displays the device exhibits a good capacitive behavior with nearly rectangular-shape CV curves without obvious redox peaks, even operating voltage up to 2.0 V. Moreover, the charge/discharge curve still preserve nearly symmetric at the operation voltage as high as 2.0 V (Figure 4c), suggesting at the voltage 2.0 V the device exhibits ideal capacitive character with a rapid I–V response and small equivalent series resistance. Thereby, in the subsequent research we chose a working voltage of 2.0 V.

The rectangular shape of CV curve at sweep rate as high as 400 mV s^{-1} still maintains well (Figure S9a), meanwhile, the charge/discharge curves at different current densities with the operation voltage of 2.0 V are almost symmetric (Figure S9b), demonstrating the asymmetric supercapacitor exhibits a desirable fast charge/discharge property.[5] From the variation of IR drop (IR_{drop}) at different discharge current densities (Figure 4d), we can reasonably infer the asymmetric supercapacitor has small internal resistance (IR_{drop} [V] = 0.01094 + $\dfrac{0.00695}{M} I$ [A]), which favors high discharge power delivery in practical applications. Moreover, the Ragone plots (Figure 4e) obtained from Figure S9b,c clearly shows the asymmetric supercapacitor has significant enhancements in both energy density and power density than p-BC@MnO$_2$-2h//p-BC@MnO$_2$-2h. And the maximum energy density of this asymmetric device (32.91 Wh kg^{-1}) is much higher than that of p-BC/N-5M//p-BC/N-5M and p-BC//p-BC. The value is also much larger than those of symmetrical supercapacitor and containing-carbon MnO$_2$ nanocompound asymmetric supercapacitors (see Supporting Information Table S2). Such a high energy density of our asymmetric capacitor is mainly attributed to the large work voltage and capacitances of two electrodes.[12] To show the practical application of p-BC@MnO$_2$-2h//p-BC/N-5M, we connected our prototype device with a red LED and successfully lighted it (Figure 4f). More importantly, the LED was on for 90 s after being charged for 44 s at 2.0 V (see Supporting Information

movie S1). Furthermore, the asymmetric device can deliver a maximum power density of 284.63 $kW \cdot kg^{-1}$, which surpasses most of the other reported MnO_2-based supercapacitors.[5,12,24] Additionally, the device exhibits a good electrochemical stability with ~95.4% retention of initial specific capacitance after 2000 cycles (see Supporting Information Figure S9d). The outstanding capacitive properties of p-BC@MnO_2-2h//p-BC/N-5M can be ascribed to the use of high conductivity aqueous electrolyte and two synergetic asymmetric electrodes without any binding agents; the ultrathin MnO_2 coating on p-BC affords more electrochemically active surface area for fast and reversible Faradic reaction, meanwhile the negative electrode of p-BC/N-5M provides much faster electron transfer, resulting in the enhancement of work voltage.

In summary, we have developed a simple, scalable, cost-effective, and green approach to fabricate one binder-free asymmetric supercapacitor with p-BC@MnO_2-2h as positive electrode material, p-BC/N-5M as negative electrode material. The optimal device can be reversibly charged/discharged at an operation voltage of 2.0 V in 1.0 M Na_2SO_4 aqueous electrolyte, delivering a high energy density of 32.91 Wh kg^{-1} and a maximum power density of 284.63 kW kg^{-1}, possessing a remarkable cycling stability with ~95.4% capacity remained after 2,000 continuous cycles. These exciting results demonstrate such relatively easy-synthesis, low-cost, and macroscopic-scale electrode materials have great potential in the fabrication of high-class supercapacitor devices for practical applications.

References

[1] L. Zhao, L. Z. Fan, M. Q. Zhou, H. Guan, S. Qiao, M. Antonietti, M. M. Titirici, *Adv. Mater.* **2010**, *22*, 5202.
[2] P. Simon, Y. Gogotsi, *Nat. Mater.* **2008**, *7*, 845.
[3] J. R. Miller, P. Simon, *Science* **2008**, *321*, 651.
[4] Y. Zhai, Y. Dou, D. Zhao, P. F. Fulvio, R. T. Mayes, S. Dai, *Adv. Mater.* **2011**, *23*, 4828.
[5] Z. J. Fan, J. Yan, T. Wei, L. J. Zhi, G. Q. Ning, T. Y. Li, F. Wei, *Adv. Funct. Mater.* **2011**, *21*, 2366.

[6] Z. S. Wu, W. C. Ren, D. W. Wang, F. Li, B. L. Liu, H. M. Cheng, *Acs Nano* **2010**, *4*, 5835.

[7] S. W. Lee, J. Kim, S. Chen, P. T. Hammond, Y. Shao-Horn, *Acs Nano* **2010**, *4*, 3889.

[8] L. F. Chen, X. D. Zhang, H. W. Liang, M. Kong, Q. F. Guan, Z. Y. Wu, S. H. Yu, *Acs Nano* **2012**, *6*, 7092.

[9] D. Hulicova-Jurcakova, A. M. Puziy, O. I. Poddubnaya, F. Suárez-García, J. M. D. Tascón, G. Q. Lu, *J. Am. Ceram. Soc.* **2009**, *131*, 5026.

[10] H. M. Jeong, J. W. Lee, W. H. Shin, Y. J. Choi, H. J. Shin, J. K. Kang, J. W. Choi, *Nano Lett.* **2011**, *11*, 2472.

[11] Q. Zhang, J. P. Rong, D. S. Ma, B. Q. Wei, *Energy Environ. Sci.* **2011**, *4*, 2152.

[12] Z. B. Lei, J. T. Zhang, X. S. Zhao, *J. Mater. Chem.* **2012**, *22*, 153.

[13] T. Brousse, P. L. Taberna, O. Crosnier, R. Dugas, P. Guillemet, Y. Scudeller, Y. Zhou, F. Favier, D. Belanger, P. Simon, *J. Power Sources* **2007**, *173*, 633.

[14] H. Jiang, J. Ma, C. Z. Li, *Adv. Mater.* **2012**, *24*, 4197.

[15] D. G. Ivey, W. W. Wei, W. F., X. W. Cui, W. X. Chen, *Chem. Soc. Rev.* **2011**, *40*, 1697.

[16] Z. Chen, Z. Jiao, D. Pan, Z. Li, M. Wu, C.-H. Shek, C. M. L. Wu, J. K. L. Lai, *Chem. Rev.* **2012**, *112*, 3833.

[17] X. Y. Lang, A. Hirata, T. Fujita, M. W. Chen, *Nat. Nanotechnol.* **2011**, *6*, 232.

[18] A. E. Fischer, M. P. Saunders, K. A. Pettigrew, D. R. Rolison, J. W. Long, *J. Electrochem. Soc.* **2008**, *155*, A246.

[19] A. E. Fischer, K. A. Pettigrew, D. R. Rolison, R. M. Stroud, J. W. Long, *Nano Lett.* **2007**, *7*, 281.

[20] G. Yu, L. Hu, M. Vosgueritchian, H. Wang, X. Xie, J. R. McDonough, X. Cui, Y. Cui, Z. Bao, *Nano Lett.* **2011**, *11*, 2905.

[21] B. G. Choi, M. Yang, W. H. Hong, J. W. Choi, Y. S. Huh, *Acs Nano* **2012**, *6*, 4020.

[22] C. J. Xu, H. D. Du, B. H. Li, F. Y. Kang, Y. Q. Zeng, *J. Electrochem. Soc.* **2009**, *156*, A435.

[23] G. P. Wang, L. Zhang, J. J. Zhang, *Chem. Soc. Rev.* **2012**, *41*, 797.

[24] X. Zhao, L. Zhang, S. Murali, M. D. Stoller, Q. Zhang, Y. Zhu, R. S. Ruoff, *Acs Nano* **2012**, *6*, 5404.

[25] Z. China Patent, *Vol. Chinese Patent, ZL96100534.3*, China.

[26] H. W. Liang, Q. F. Guan, Z. Zhu, L. T. Song, H. B. Yao, X. Lei, S. H. Yu, *NPG Asia Mater.* **2012**, DOI:10.1038/am.2012.34.

[27] H. Yano, J. Sugiyama, A. N. Nakagaito, M. Nogi, T. Matsuura, M. Hikita, K. Handa, *Adv. Mater.* **2005**, *17*, 153.

[28] M. Toupin, T. Brousse, D. Bélanger, *Chem. Mater.* **2004**, *16*, 3184.

[29] Y. Zhu, S. Murali, M. D. Stoller, K. J. Ganesh, W. Cai, P. J. Ferreira, A. Pirkle, R. M. Wallace, K. A. Cychosz, M. Thommes, D. Su, E. A. Stach, R. S. Ruoff, *Science* **2011**, *332*, 1537.

[30] L. Bao, J. Zang, X. Li, *Nano Lett.* **2011**, *11*, 1215.

[31] F. Su, C. K. Poh, J. S. Chen, G. Xu, D. Wang, Q. Li, J. Lin, X. W. Lou, *Energy Environ. Sci.* **2011**, *4*, 717.

[32] L. Sun, L. Wang, C. G. Tian, T. X. Tan, Y. Xie, K. Y. Shi, M. T. Li, H. G. Fu, *RSC Adv.* **2012**, *2*, 4498.

[33] H. Jiang, C. Z. Li, T. Sun, J. Ma, *Nanoscale* **2012**, *4*, 807.

[34] V. Khomenko, E. Raymundo-Pinero, F. Beguin, *J. Power Sources* **2006**, *153*, 183.

Supporting Information

Bacterial Cellulose Derived Carbon Nanofiber@MnO$_2$ and Nitrogen-Doped Carbon Nanofiber Electrode Materials: Asymmetric Supercapacitor with High Energy and Power Density

Li-Feng Chen, Zhi-Hong Huang, Hai-Wei Liang, Qing-Fang Guan, Shu-Hong Yu*

Experimental Section

Purified bacterial cellulose (BC) pellicles (thickness: 3.0 mm) were kindly provided by Ms. C.Y. Zhong (Hainan Yeguo Foods Co., Ltd., China). All other chemicals were analytical grade and commercially available from Shanghai Chemical Reagent Co. Ltd and used as received without further purification.

Preparation of p-BC: The BC pellicles were first cut into some squares, then frozen in liquid nitrogen (−196 °C), subsequently freeze-dried in a bulk tray dryer (Labconco Corporation, USA) at a sublimating temperature of −48 °C and a pressure of 0.04 mbar. The obtained BC was then pyrolyzed under flowing N$_2$ atmosphere at 1000 °C for 2.0 h to generate a black *p*-BC (the yield of *p*-BC by pyrolysis of bacterial cellulose is about 5.63 wt %).

Incorporation of MnO$_2$ into p-BC pellicles: The *p*-BC pellicles were dipped into 0.1 M KMnO$_4$/0.1 M K$_2$SO$_4$ solution for 0.5, 1.5, 2.0, and 2.5 h at room temperature within the shaking table, leading to the samples denoted as *p*-BC@MnO$_2$-xh (x = 0.5, 1.5, 2.0, 2.5).

Preparation of p-BC/N pellicles: Typically, 40 mg *p*-BC was immersed in 40.0 mL of 5.0 M urea aqueous solution for 30 min at room temperature. Then, the mixture was transferred into a 50 mL of Teflon-lined stainless steel autoclave and maintained at 180 °C for 12 h. Finally, the as-prepared sample was washed with deionized water and alcohol for several times before freeze-dried. For comparison, the *p*-BC/N-yM (y = 3, 4, 6) was also synthesized under the same condition.

Characterizations. SEM was performed with a field emission scanning electron microanalyzer (Zeiss Supra 40) at an acceleration voltage of 5 kV. Transmission electron microscope (TEM) images were performed on a Hitachi H7650 transmission electron microscope with CCD imaging system on an

acceleration voltage of 120 kV. High-resolution transmission electron microscope (HRTEM), scanning TEM images (STEM) and elemental mapping were obtained on a JEOL-2010 transmission electron microscope at an acceleration voltage of 200 kV. X-ray diffraction (XRD) data were characterized on a Philips X'Pert Pro Super X-ray diffractometer equipped with graphite monochromatized Cu Kα radiation (λ = 1.54184Å). Raman scattering spectra were obtained on a Renishaw System 2000 spectrometer using the 514.5 nm line of Ar$^+$ for excitation. X-ray photoelectron spectra (XPS) were determined on an X-ray photoelectron spectrometer (ESCALab MKII) with an excitation source of Mg Kα radiation (1253.6 eV). N_2 sorption analysis was recorded from an ASAP 2020 accelerated surface area and porosimetry instrument (Micromeritics), equipped with automated surface area, at 77 K using Barrett−Emmett−Teller (BET) calculations for the surface area. The pore size distribution (PSD) plot was conducted on the adsorption branch of the isotherm based on Barrett−Joyner−Halenda (BJH) model. The mass percentage of MnO_2 coating on the *p*-BC was carried out by the inductively coupled plasma-atomic emission spectrometry (ICP-AES) analysis using an Atomscan Advantage (Thermo Ash Jarrell Corporation, USA) spectrometer.

Electrochemical Measurement. A two-electrode configuration consists of two slices of electrode material with the same size (about 1 cm by 1 cm), a cellulose acetate membrane (porous size of 225 nm) as separator, and two pieces of nickel foil as the current collectors. Then, the cell assemblies were wrapped with parafilm. Before the construction of assemblies, the electrodes were soaked in the 1.0 M Na_2SO_4 aqueous electrolyte for 3 h.

All of the capacitive performances was performed on a CHI 760D electrochemical workstation in the 1.0 M Na_2SO_4 solution. In the symmetric supercapacitors (*p*-BC//*p*-BC, *p*-BC/N-yM//*p*-BC/N-yM, and *p*-BC@MnO$_2$-xh//*p*-BC@MnO$_2$-xh), the total electrode material mass of the *p*-BC, *p*-BC/N-yM, and *p*-BC@MnO$_2$-xh was 0.9 ± 0.1, 0.9 ± 0.1, and 1.2 ± 0.1 mg, respectively. To construct the asymmetric supercapacitors, 0.6 mg *p*-BC@MnO$_2$-2h pellicle was used for the positive electrode and the negative electrode was 0.9 mg *p*-BC/N-5M pellicle. The area of the active material on each electrode was about 1.0 cm × 1.0 cm. The electrochemical performance of samples was determined by the cyclic voltammetry (CV) and galvanostatic charge-discharge. All electrochemical experiments were carried out at room temperature.

Specific capacitance values of the electrode composites were calculated from the galvanostatic discharge process according to the following equation:[1-3]

$$C_s = \frac{4I \times \Delta t}{m \times \Delta V} \qquad (1)$$

where C_s (F g^{-1}) represents specific capacitance of the electrode material, I (A) corresponds to the discharge current, ΔV (V) is the potential change within the discharge time Δt (s), and m (g) refers to the total mass of active material on the two electrodes of the capacitor.

Specific capacitance of the asymmetric supercapacitors were calculated *via* the following equation:[4-5]

$$C_m = \frac{I \times \Delta t}{M \times \Delta V} \qquad (2)$$

where C_m (F g^{-1}) is specific capacitance of the supercapacitor, I (A) corresponds to the discharge current, ΔV (V) is the potential change within the discharge time Δt (s), and M (g) refers to the total mass of active materials on the two electrodes. Note that the specific capacitance of the asymmetric supercapacitor is calculated using the total mass of active materials on two electrodes.

The key parameters of the supercapacitor, power density (P) and energy density (E), were calculated using eqs. (3) and (4).[3, 5]

$$E = \frac{1}{2} \times C_m \times (\Delta V)^2 \qquad (3)$$

$$P_{av} = \frac{E}{\Delta t} \qquad (4)$$

where C_m (F g^{-1}) represents the specific capacitance of the supercapacitor measured from the eqs. (2), ΔV (V) refers to the potential change within the discharge time Δt (s), E (J g^{-1}) is the energy density, P_{av} (W g^{-1}) is the average power density.

The maximum specific power was calculated using the R_s value obtained from a linear fitting to the IR_{drop} values according to eqs. (5) and (6):[6]

$$IR_{drop} = a + bI \qquad (5)$$

$$P_{max} = \frac{V_0^2}{4M \times R_s} = \frac{(2-a)^2}{2M \times b} \qquad (6)$$

where a represents the difference between the applied potential of 2 V and the charged potential of the capacitor, b means double the value of the internal resistance R_s (Ω), and I (A) is the discharge current, P_{max} (W g^{-1}) refers to the maximum power density, V_0 represents the practical work potential of the

device, M (g) means the total mass of the electrode material in the device.
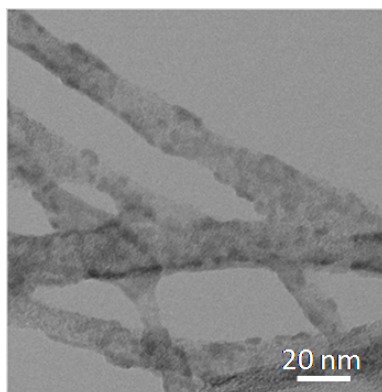
Figure S1. Typical high-resolution STEM image of p-BC@MnO$_2$-2h.
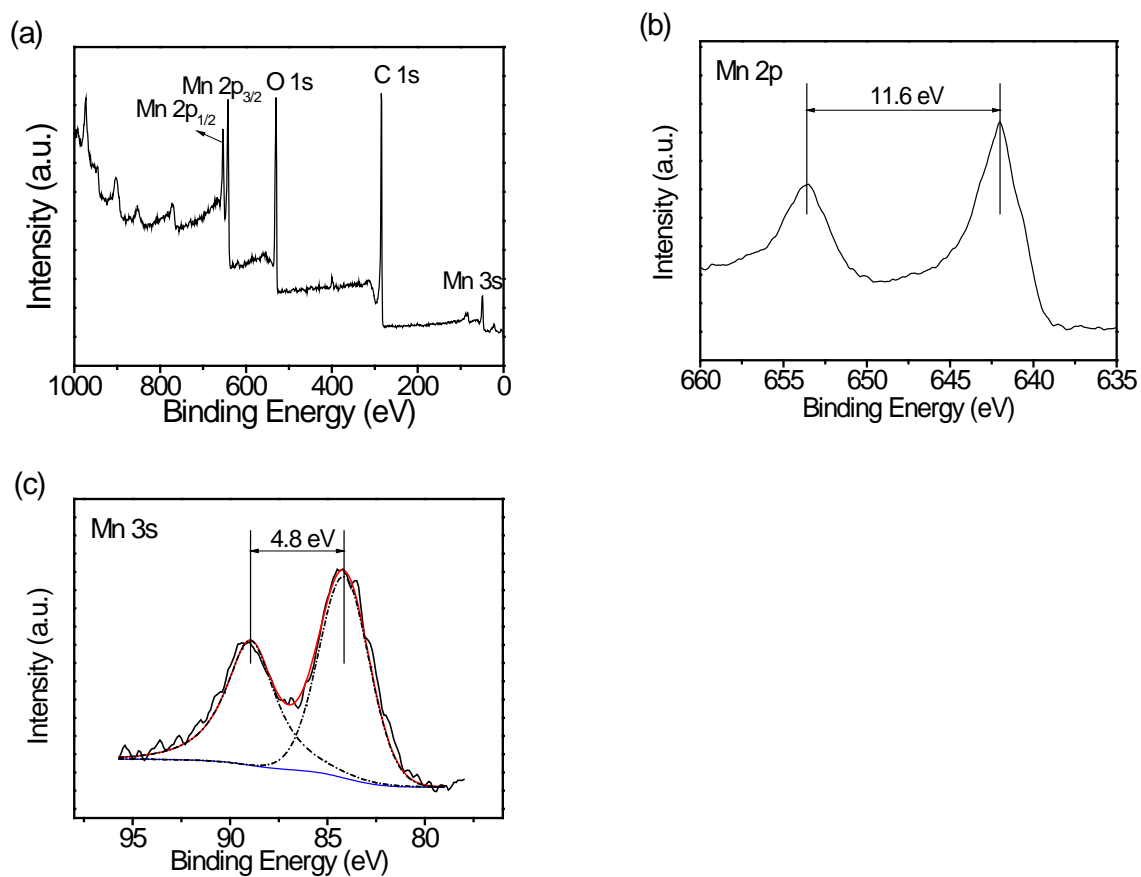
Figure S2. XPS spectra of p-BC@MnO$_2$-2h. (a) XPS survey spectra. (b,c) High-resolution XPS spectra of (b) Mn 2p and (c) Mn 3s. Two characteristic peaks in the Mn 2p spectrum at 653.6 and 642.0 eV are assignable to Mn 2p$_{3/2}$ and Mn 2p$_{1/2}$ spin-orbit peaks of MnO$_2$, respectively.[7]
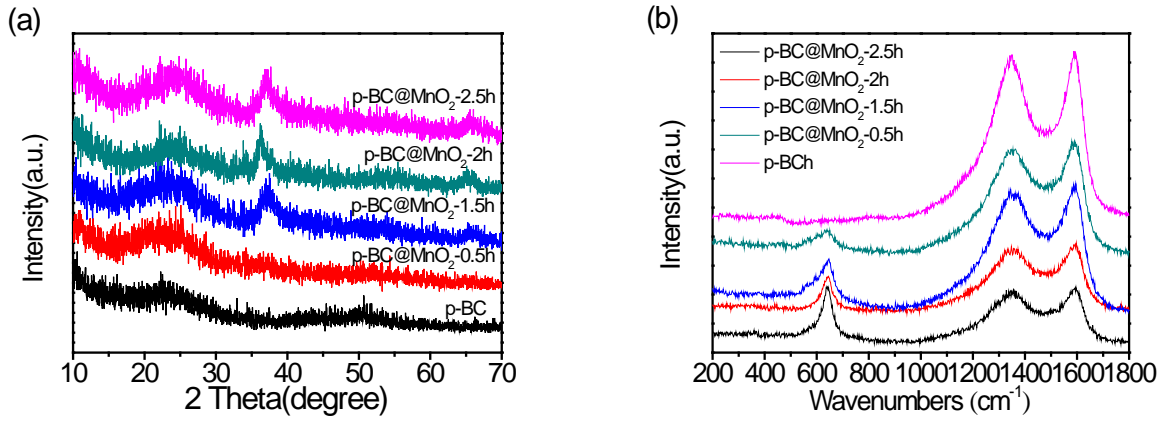
Figure S3. (a) XRD spectra of *p*-BC and *p*-BC@MnO$_2$ nanocomposites. The broad peak at 2θ = 21.98° indicates the *p*-BC consists of graphitized carbon as a result of the carbonization of the BC. The most relevant characteristic peaks of *p*-BC@MnO$_2$ nanocomposites at 2θ = 24, 37, and 66° can be indexed to birnessite-type MnO$_2$ (JCPDS 42-1317).[8] (b) Raman spectra of *p*-BC and *p*-BC@MnO$_2$. The peaks at about 1593 and 1350 cm^{-1} are G-band and D-band, respectively; [5, 8] in low band region, the weak band at 646 cm^{-1} is associated with the symmetric stretching vibration M–O of MnO$_6$ groups.[8]
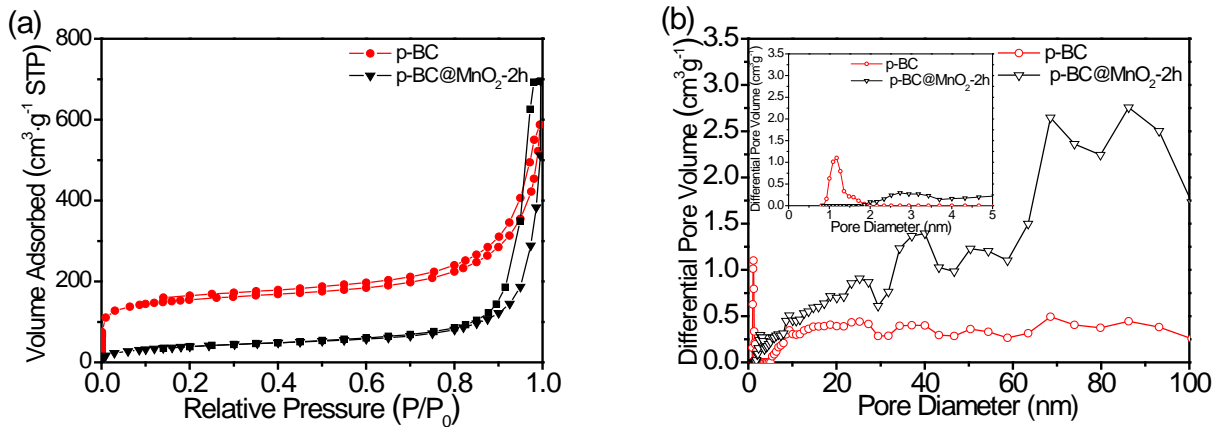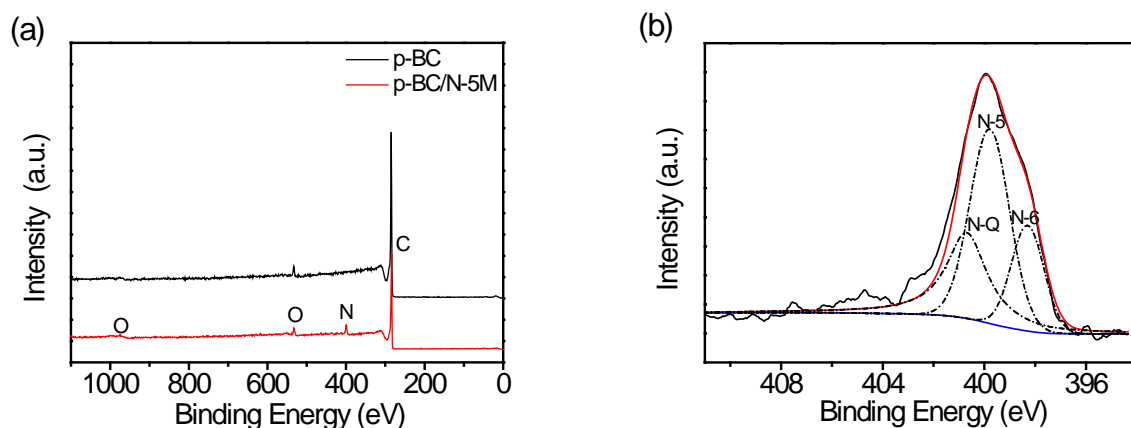

Figure S4. a) Nitrogen adsorption-desorption isotherms and b) Pore size distribution of *p*-BC and *p*-BC@MnO$_2$-2h (inset: magnified 0–10 nm region).

Table S1. Pore parameters of the prepared samples. (Calculated total surface S_{BET}, t-method external surface area S_E, total pore volume V_T, average pore diameter d_M)

| Sample	S_{BET} (m^2 g^{-1})	S_E (m^2 g^{-1})	V_T (cm^3 g^{-1})	d_M (nm)
p-BC	489.22	226.74	0.91	7.43
p-BC@MnO$_2$-2h	150.86	156.97	1.08	30.48
p-BC/N-5M	252.23	238.35	0.60	9.52
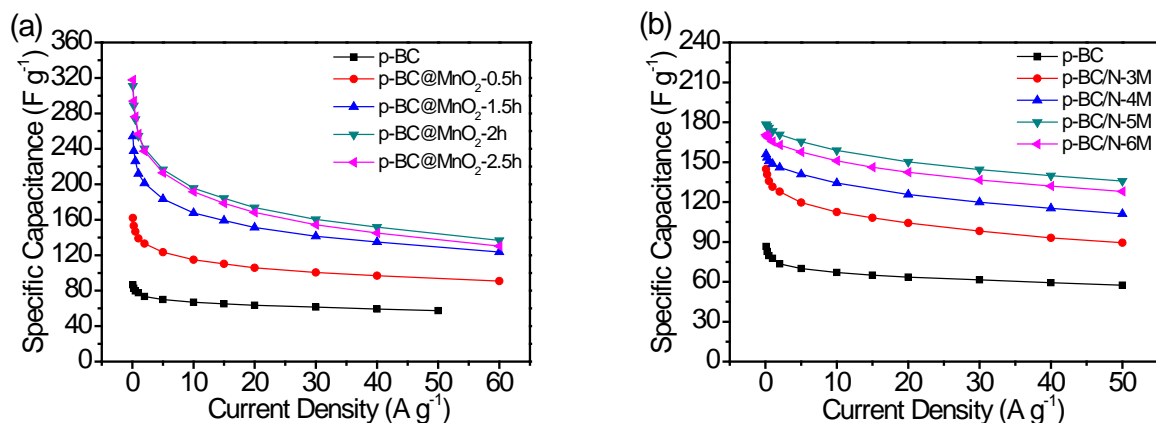
Figure S5. Electrochemical properties of the materials measured using a two-electrode system in 1.0 M Na$_2$SO$_4$ aqueous electrolyte. (a) Variation of specific capacitance of *p*-BC@MnO$_2$ and *p*-BC against current density. (b) Variation of specific capacitance of *p*-BC/N and *p*-BC against current density.

Figure S6. (a) XPS survey spectra of *p*-BC/N-5M and *p*-BC. (b) High-resolution XPS spectra of deconvoluted N1s peak of *p*-BC/N-5M.
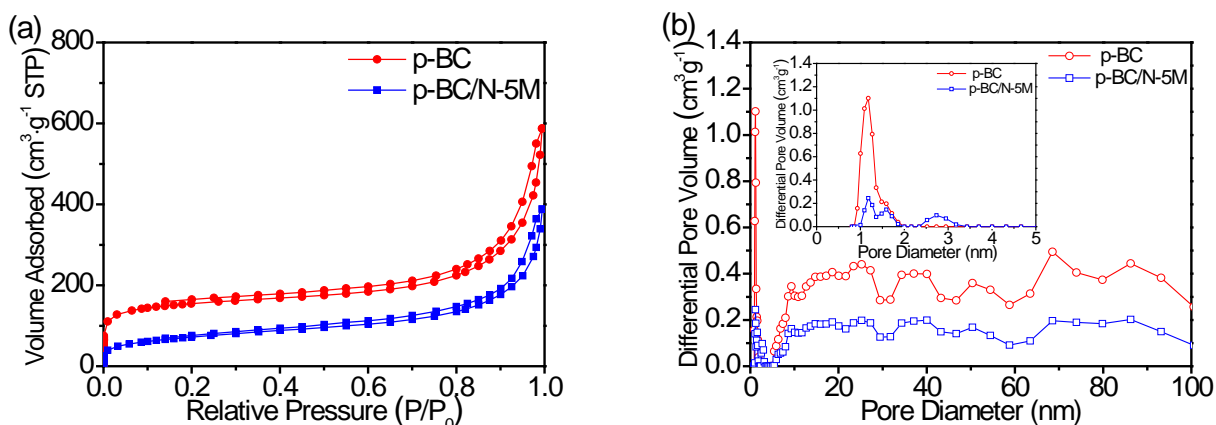
Figure S7. (a) Nitrogen adsorption-desorption isotherms and (b) Pore size distribution of *p*-BC and *p*-BC/N-5M (inset: magnified 0–10 nm region).

Figure S8. A prototype of our designed asymmetric supercapacitor *p*-BC@MnO$_2$-2h//*p*-BC/N-5M.

Table S2. Capacitive properties of the containing-MnO$_2$ supercapacitors

Capacitor	Energy density (Wh kg^{-1})	Reference
Graphene/MnO$_2$//graphene/MnO$_2$	8.5	[9]
MnO$_2$//MnO$_2$	3.3	[10]
MnO$_2$//activated carbon (AC)	<21	[11-12]
Graphene/MnO$_2$//graphene	<11.4	[9, 13]
Manganese oxide/AC//AC	21.0	[14]
CNTs/MnO$_2$//CNTs/SnO$_2$	20.3	[15]
MnO$_2$ nanowire/graphene//graphene	30.4	[16]
p-BC@MnO$_2$-2h//*p*-BC/N-5M	32.91	Present work
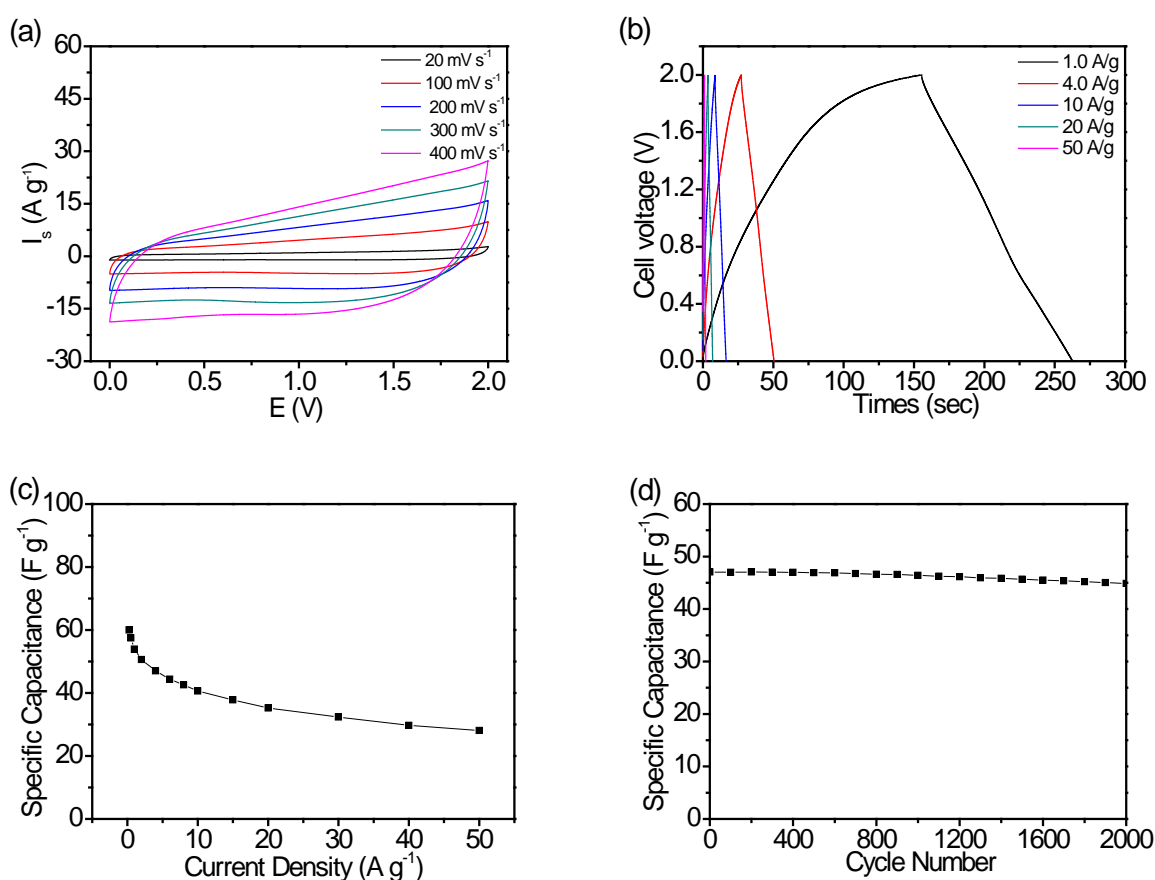
Figure S9. a) CV curves recorded with an operation voltage of 2.0 V at different scan rates. b) Galvanostatic charge–discharge curves obtained at different current densities. c) Variation of specific capacitance of the *p*-BC@MnO$_2$-2h//*p*-BC/N-5M asymmetric supercapacitor against current density. d) Cycling performance of the asymmetric supercapacitor at a current density of 4.0 A g^{-1}.

Movies: Supplementary movie S1.

Reference

[1] X. Zhao, L. Zhang, S. Murali, M. D. Stoller, Q. Zhang, Y. Zhu, R. S. Ruoff, *Acs Nano* **2012**, *6*, 5404.

[2] L. Wei, M. Sevilla, A. B. Fuertes, R. Mokaya, G. Yushin, *Adv. Funct. Mater.* **2012**, *22*, 827.

[3] Y. Zhu, S. Murali, M. D. Stoller, K. J. Ganesh, W. Cai, P. J. Ferreira, A. Pirkle, R. M. Wallace, K. A. Cychosz, M. Thommes, D. Su, E. A. Stach, R. S. Ruoff, *Science* **2011**, *332*, 1537.

[4] Z. J. Fan, J. Yan, T. Wei, L. J. Zhi, G. Q. Ning, T. Y. Li, F. Wei, *Adv. Funct. Mater.* **2011**, *21*, 2366.

[5] L. F. Chen, X. Zhang, H. W. Liang, M. Kong, Q. F. Guan, Z. Y. Wu, S. H. Yu, *Acs Nano* **2012**, *6*, 7092.

[6] A. Izadi-Najafabadi, S. Yasuda, K. Kobashi, T. Yamada, D. N. Futaba, H. Hatori, M. Yumura, S. Iijima, K. Hata, *Adv. Mater.* **2010**, *22*, E235.

[7] S. W. Lee, J. Kim, S. Chen, P. T. Hammond, Y. Shao-Horn, *Acs Nano* **2010**, *4*, 3889.

[8] Z. B. Lei, J. T. Zhang, X. S. Zhao, *J. Mater. Chem.* **2012**, *22*, 153.

[9] Q. Cheng, J. Tang, J. Ma, H. Zhang, N. Shinya, L. C. Qin, *Carbon* **2011**, *49*, 2917.

[10] T. Cottineau, M. Toupin, T. Delahaye, T. Brousse, D. Bélanger, *Appl. Phys. A Mater. Sci. Process.* **2006**, *82*, 599.

[11] T. Brousse, P. L. Taberna, O. Crosnier, R. Dugas, P. Guillemet, Y. Scudeller, Y. Zhou, F. Favier, D. Belanger, P. Simon, *J. Power Sources* **2007**, *173*, 633.

[12] C. J. Xu, H. D. Du, B. H. Li, F. Y. Kang, Y. Q. Zeng, *J. Electrochem. Soc.* **2009**, *156*, A435.

[13] L. Deng, G. Zhu, J. Wang, L. Kang, Z. H. Liu, Z. Yang, Z. Wang, *J. Power Sources* **2011**, *196*, 10782.

[14] V. Khomenko, E. Raymundo-Pinero, F. Beguin, *J. Power Sources* **2006**, *153*, 183.

[15] N. Kok Chiang, Z. Shengwen, P. Chuang, G. Z. Chen, *J. Electrochem. Soc.* **2009**, *156,* A846.

[16] Z. S. Wu, W. C. Ren, D. W. Wang, F. Li, B. L. Liu, H. M. Cheng, *Acs Nano* **2010**, *4*, 5835.